MATERIALS SCIENCE

Sustainable valorization of asphaltenes via flash joule heating

M.A.S.R. Saadi[1]†, Paul A. Advincula[2]†, Md Shajedul Hoque Thakur[1], Ali Zein Khater[1], Shabab Saad[3], Ali Shayesteh Zeraati[3], Shariful Kibria Nabil[3], Aasha Zinke[1], Soumyabrata Roy[1], Minghe Lou[4], Sravani N. Bheemasetti[5,6], Md Abdullah Al Bari[3], Yiwen Zheng[7], Jacob L. Beckham[2], Venkataramana Gadhamshetty[5,6], Aniruddh Vashisth[7], Md Golam Kibria[3]*, James M. Tour[1,2]*, Pulickel M. Ajayan[1]*, Muhammad M. Rahman[1]*

The refining process of petroleum crude oil generates asphaltenes, which poses complicated problems during the production of cleaner fuels. Following refining, asphaltenes are typically combusted for reuse as fuel or discarded into tailing ponds and landfills, leading to economic and environmental disruption. Here, we show that low-value asphaltenes can be converted into a high-value carbon allotrope, asphaltene-derived flash graphene (AFG), via the flash joule heating (FJH) process. After successful conversion, we develop nanocomposites by dispersing AFG into a polymer effectively, which have superior mechanical, thermal, and corrosion-resistant properties compared to the bare polymer. In addition, the life cycle and technoeconomic analysis show that the FJH process leads to reduced environmental impact compared to the traditional processing of asphaltene and lower production cost compared to other FJH precursors. Thus, our work suggests an alternative pathway to the existing asphaltene processing that directs toward a higher value stream while sequestering downstream emissions from the processing.

INTRODUCTION

The technological and cultural advancement of human civilization entails a continuous supply of energy, and no energy source has been as enabling as fossil fuels for the past century. Of the fossil fuels, petroleum oil accounts for the majority share (~33 to 34%) (*1*), thus serving as one of the primary sources of energy throughout the world. Hydrocarbon-enriched crude oil formed underground, or crude bitumen naturally existing as consolidated oil sands, is extracted and refined in petroleum industries into "cleaner" fuels. The refining scheme generally involves fractional and continuous distillation processes and generates substantial quantities of residues and/or by-products. Asphaltenes are heavy macromolecules present in the high-temperature residuum of the distillation process. During the refining process, these molecules tend to migrate with crude oils to reservoirs (*2*), precipitate out (*3*), disrupt catalytic reactions (*4*), and act as coke precursors (*4*, *5*) while increasing the viscosity of heavy oil (*5*), thus impeding the crude oil processing and lowering the economic value of the crude oil. Consequently, asphaltenes are deemed as low-value by-products with little to no real-world application and commercial use in today's market.

Worldwide reserves of asphaltenes are currently estimated to be ~1 to 2 trillion barrels (*6*). Poor biodegradability (*7*), ignitability (*8*), and reactivity (*9*) of this enormous amount of by-product raise concerns over their reuse and/or disposal. Isolated via conventional separation techniques, asphaltenes are typically combusted for reuse as transportation fuels and/or discarded in tailing ponds and landfills (*10*–*12*). While adding to the cost and energy expenses, asphaltene combustion becomes critically responsible for the emission of increased greenhouse gases and carbon footprint. On the other hand, improper disposal of asphaltene into landfills and tailing ponds can simultaneously pollute the air, water, and soil (*3*, *5*). Evidently, existing recycling processes of asphaltene pose roadblocks to achieving net-zero emission goals. Hence, scalable and sustainable valorization of this material can be critical to addressing the ongoing ecological disruption.

Asphaltenes are rich in carbon (~70 to 80%), and such a carbon-rich material with diverse and appealing physicochemical characteristics, for example, high aromaticity, heteroatom content, polar functional groups, and double bond equivalent numbers, can have great potential as an inexpensive and readily available feedstock for developing carbon-based structural and functional materials (*5*, *13*). Consequently, research on the valorization of asphaltenes has sparked over the past few years. To date, efforts have been invested in developing carbon fibers (*6*), carbon electrodes (*5*, *14*), porous carbon foam/scaffolds (*15*), and carbon nanosheets (*16*, *17*) from asphaltenes. However, a green recycling or upcycling solution that will simultaneously convert low-value asphaltene into high-value carbon materials/allotropes and develop end products appropriate for a myriad of engineering applications is still unrealized.

Here, we report the bulk-scale conversion of asphaltenes into a stable, naturally occurring form of carbon, namely, graphene, using a single-step, low-cost, energy-efficient, recyclable, scalable, and sustainable technique called flash joule heating (FJH) (*18*). The process uses no furnace, solvents, or reactive gases and, in less than 1 s, produces what is called asphaltene-derived flash graphene (AFG), having a turbostratic configuration between the stacked graphene layers and very low defect concentration. The conversion process is systematically evaluated and confirmed by conducting extensive physicochemical characterization, including Raman spectroscopy, thermogravimetric analysis (TGA), x-ray photoelectron spectroscopy (XPS), x-ray diffraction (XRD) spectroscopy, and high-resolution transmission electron

[1]Department of Materials Science and NanoEngineering, Rice University, Houston, TX 77005, USA. [2]Department of Chemistry, Rice University, Houston, TX 77005, USA. [3]Department of Chemical and Petroleum Engineering, University of Calgary, Calgary, AB T2N 1N4, Canada. [4]Department of Electrical and Computer Engineering, Rice University, Houston, TX 77005, USA. [5]Department of Civil and Environmental Engineering, South Dakota School of Mines and Technology, Rapid City, SD 57701, USA. [6]Two-Dimensional Materials for Biofilm Engineering Science and Technology (2D-BEST) Center, South Dakota Mines, Rapid City, SD 57701, USA. [7]Department of Mechanical Engineering, University of Washington, Seattle, WA 98195, USA.
*Corresponding author. Email: md.kibria@ucalgary.ca (M.G.K.); tour@rice.edu (J.M.T.); ajayan@rice.edu (P.M.A.); maksud@rice.edu (M.M.R.)
†These authors contributed equally to this work.

microscopy (HR-TEM). We also conduct atomistic simulations for a deeper understanding of the conversion process. Next, we develop polymer-AFG nanocomposites with varying AFG concentrations using a mold casting technique, which shows improved mechanical and thermal properties compared to bare polymer, thus showcasing its reinforcing effect. We also show that complex architected nanocomposites can be fabricated via additive manufacturing (AM) techniques by tuning the rheology of the polymer-AFG mix. Furthermore, we investigate the electrochemical performance of the polymer-AFG nanocomposites to evaluate the corrosion behavior and obtain unique anticorrosion properties. Last, the life cycle assessment (LCA) reveals that replacing the existing combustion of asphaltenes with FJH substantially reduces carbon emissions. On the other hand, the technoeconomic analysis reveals a very low production cost of AFG compared to flash graphene produced from other FJH precursors and graphene synthesized by conventional chemical vapor deposition (CVD) techniques. This work thereby presents a comprehensive technological scheme (Fig. 1) for transforming a petroleum by-product into high-value carbon-based materials suitable for broader engineering applications. Thus, it suggests a pathway towards improved economic and ecological sustainability.

RESULTS

FJH of asphaltene

The FJH process is a resistive/ohmic heating process that requires the source material to be electrically conductive (*18*). Asphaltene being a poor conductor, a minimal amount [20 weight % (wt %)] of conductive carbon black (CB) is added to the raw asphaltene powder. Note that the CB can be substituted with AFG from a former run or metallurgical coke (fig. S1). The conductive homogeneous mixture is lightly compressed inside a quartz tube between two copper electrodes. High-voltage electric discharge (table S1 and fig. S2) from a capacitor bank brings the source mixture to temperatures higher than 3000 K in less than 100 ms (Fig. 1B), effectively converting into AFG with a process yield of ~45% and an AFG yield above 95%. Note that the process yield is calculated as the ratio of AFG mass to the initial mass of the CB:asphaltene feedstock, while the AFG yield is based on the percentage of Raman spectroscopic signals that showed graphene-like signatures (*19*). Details of Raman spectroscopic analysis will be explained in the following section.

Structure, composition, and morphology of AFG

Raman spectroscopy is a versatile tool to identify and characterize the chemical and physical properties of graphene-based materials (*20*). It provides critical structural information about the layered material by comparing the intensity ratios of various peaks. These peaks include the D, G, and 2D bands, which appear at ~1350, ~1580, and ~2700 cm^{-1}, respectively. The average Raman spectrum of AFG has an I_{2D}/I_G ratio of 0.941 and an I_D/I_G ratio of 0.244 (Fig. 2A). The low intensity of the D band indicates low defect concentration in AFG, which also contributes to the amplification of the 2D band. Successful conversion to AFG was contingent upon the following criteria used in our Raman spectral analysis: (i) a minimum I_{2D}/I_G ratio of 0.3, (ii) a signal-to-noise ratio of >5 in the 2D band region, and (iii) a 2D band full width at half maximum (FWHM) of <100 cm^{-1}. On the basis of these criteria, 97.9% of the Raman spectra indicated successful conversion of asphaltene into high-quality graphene. In addition, the standard deviation (SD, shown as shaded regions) reveals that the sample is relatively homogeneous. TGA (Fig. 2B) also corroborates the conversion of the feedstock from asphaltene into AFG (*21*). The initial asphaltene feedstock begins to degrade at ~350°C and is completely degraded at ~550°C. In contrast, AFG remains stable until ~500°C, with minimal degradation before this point, indicating that no asphaltene remains after FJH conversion. By ~725°C, almost all the AFG is completely degraded. This shows that after FJH, asphaltenes are mostly converted into AFG, evidenced by their increased degradation temperature.

To characterize the chemical composition, XPS was performed on the synthesized AFG. XPS survey of asphaltene and AFG shows that carbon percentage increased from ~93 to ~99% after the conversion process. Moreover, the initial feedstock of asphaltene contains heteroatoms such as oxygen and sulfur; however, the FJH process significantly reduces the number of heteroatoms present. The survey spectra (Fig. 2C) showed that the oxygen content dropped from ~4 to ~1%, while the sulfur content decreased from ~2.6% for asphaltene to almost zero for AFG. To obtain a deeper understanding of the chemical structure, the high-resolution XPS core level spectra for asphaltene and AFG (Fig. 2, D and E, and fig. S3) were analyzed. The high-resolution C1s spectrum for asphaltene (Fig. 2D) can be fitted to four components centered about 284.7, 285.7, 286.6, and 287.8, which are attributed to C─C/C═C, C─O─C/C─S, C═O/C═S, and O═C─O, respectively. On the other hand, the high-resolution C1s peaks for AFG can be deconvoluted into three peaks corresponding to C─C/C═C, C─O─C, and C═O at 284.8, 285.5, and 286.3 eV, respectively, as shown in Fig. 2E.

The XRD pattern of AFG (Fig. 2F) shows a well-defined (002) peak indicating successful graphitization of the asphaltene. The (002) peak of AFG that appears at 26.1° shows an increased FWHM and a slightly higher diffraction angle than that of AB-stacked graphite nanoplatelets (*22*), indicating the expanded and turbostratic structure of AFG. The (002) peak of AFG has a tail extending to low 2θ due to rotational disorder between the AFG layers. In addition, the decreased intensity of three-dimensional (3D) peaks (101) and (102) that appear at 45° and 50°, respectively, indicates turbostratic structure (*23*). To visualize the morphology and structure of AFG, we used HR-TEM, and two representative images are displayed in Fig. 2 (G and H). The average lateral size of AFG particles estimated (fig. S4) from the acquired HR-TEM images was found to be ~25.4 nm with an SD of 7.4 nm, as shown in Fig. 2I. Measurement of the lattice edges of the AFG particles shows that the average interlayer spacing is ~0.359 nm with an SD of 0.041 nm (fig. S4). This is higher than the interlayer spacing found in a typical Bernal (AB-stacked) graphene (~0.335 nm). The increased interlayer spacing of AFG is again due to the turbostratic nature of the material.

To better understand the mechanism of the rapid conversion of asphaltene to AFG, we perform reactive force-field (ReaxFF) molecular dynamics simulation (Fig. 2J) (*24*–*26*). The simulation box (details can be found in Materials and Methods) consisted of two types of molecules: (i) asphaltene and (ii) polycrystalline carbon that emulates the CB used in the experiment (fig. S5). Overall, we see that the carbon atoms in the system transition from sp^3 to sp^2 hybridization; this is captured by the radial distribution function (rdf) calculations (Fig. 2K). It can be seen that more sp^2 carbons are populated on the AFG molecule compared to the initial asphaltene molecule. We found that during the simulation process, the polycrystalline carbon acts as a nucleating agent, and the AFG molecules start to grow around it (movie S1). A similar phenomenon was observed in the study by

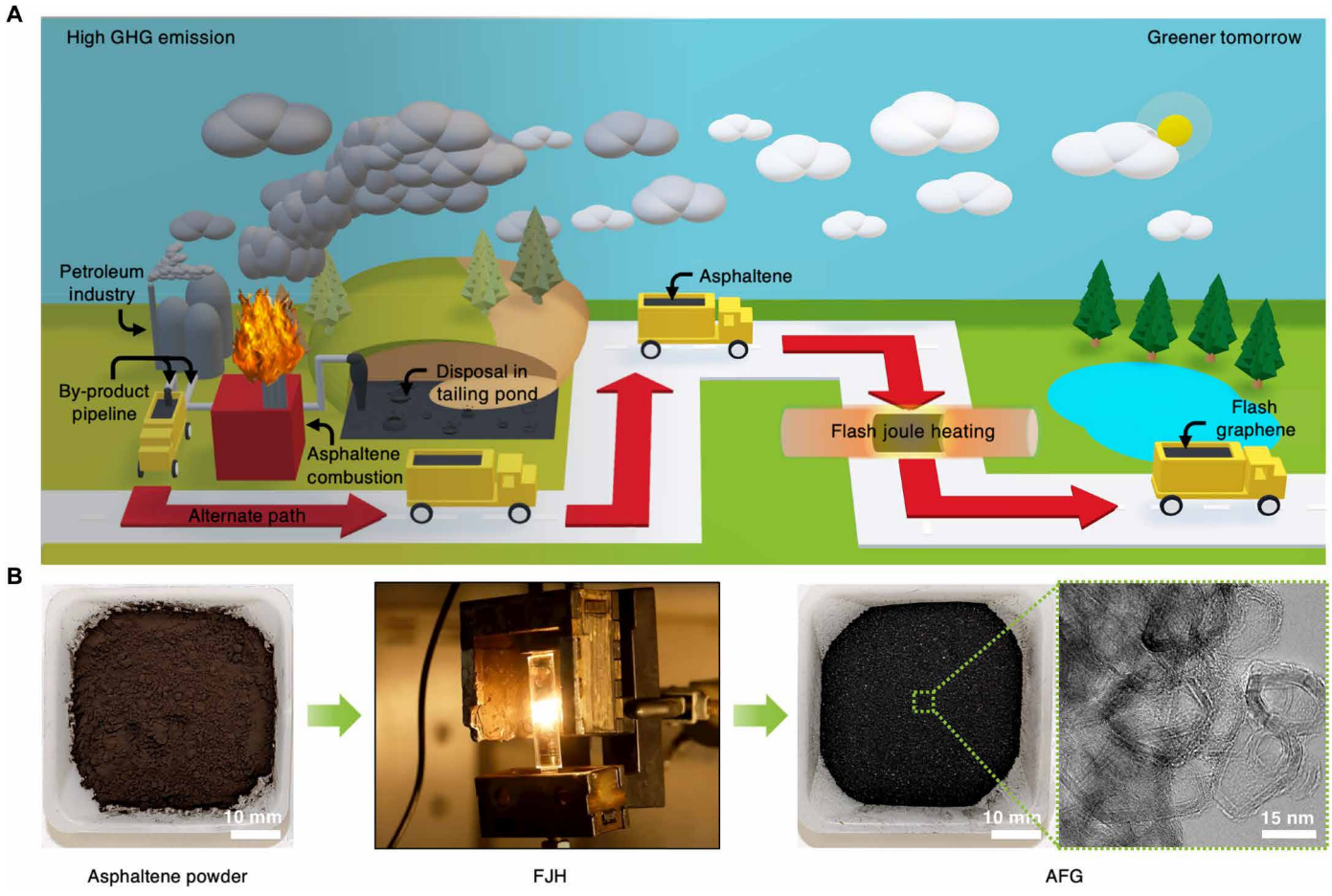

Fig. 1. Flash graphene from asphaltenes. (**A**) Schematic conceptualization of sustainable valorization of asphaltene. (**B**) Photograph of ground asphaltene powder, the FJH jig during a flash treatment event, AFG, and a TEM image of the AFG flakes.

Zang *et al.* (*27*) in that upon laser upgrading of heavy hydrocarbons, the existence of built-in aromatics was crucial to induce graphitic stacking, while the alkane chains supplied carbon to the original aromatic sheets by dehydrogenation. From the simulation, we also found that three main species of gases are released during the conversion process, namely, carbon monoxide (CO), hydrogen (H_2), and acetylene (C_2H_2) (fig. S6). Other compounds ($C_xH_yN_z$) are also released as the reaction progresses. The sp peak in the rdf calculations can be related to C_2H_2 gases being evolved during the conversion. Note that the evolution of CO and C_2H_2 plateaus out after the initial ramp up, but the continuous release of H_2 molecules and the rearrangement of the carbon molecules lead to a higher sp^2 character in the AFG molecule. The final flash graphene structure (movie S2) had five-, six-, and seven-member carbon rings (fig. S6), which give it a nonplanar configuration.

Mechanical properties and advanced manufacturability

After the successful conversion, we have used AFG in various polymer nanocomposite applications. First, we investigated their effect as reinforcement in a polymer matrix. In this work, epoxy resin was used as the matrix phase because epoxies are widely regarded for their good mechanical properties, chemical resistance, low cost, and versatile polymerization routes (*28*). The turbostratic nature of AFG makes it suitable for use in polymer composites since the reduced van der Waals interactions from the increased spacing and rotation between sheets make AFG easier to exfoliate and disperse (*18*). As a result, with mild sonication and without using any surfactant, effective dispersion of AFGs in the epoxy matrix could be achieved. The approach used to disperse AFG in the thermosetting epoxy and fabricate the epoxy-AFG nanocomposites with varying AFG concentrations is discussed in detail in the Supplementary Materials. To investigate the mechanical properties critical for any structural application, we compared the tensile strength, Young's modulus, and toughness of the nanocomposites with 1, 3, and 5 wt % AFG loading. The results of the uniaxial tensile testing of the pure epoxy and nanocomposite samples are shown in Fig. 3.

Figure 3A shows representative stress-strain plots of the polymer and nanocomposite samples, while Fig. 3 (B and C) shows the fracture surface of the neat epoxy and epoxy-AFG (1 wt %) nanocomposite after the tensile test, seen under a scanning electron microscope (SEM). The comparison of the tensile strength, Young's modulus, and toughness is presented in Fig. 3 (D to F, respectively). Figure 3 (D and E) shows that the tensile strength and Young's modulus of the nanocomposites increased with 1 wt % AFG reinforcement compared to neat epoxy. The maximum increase in tensile strength was ~37%, while Young's modulus increased up to

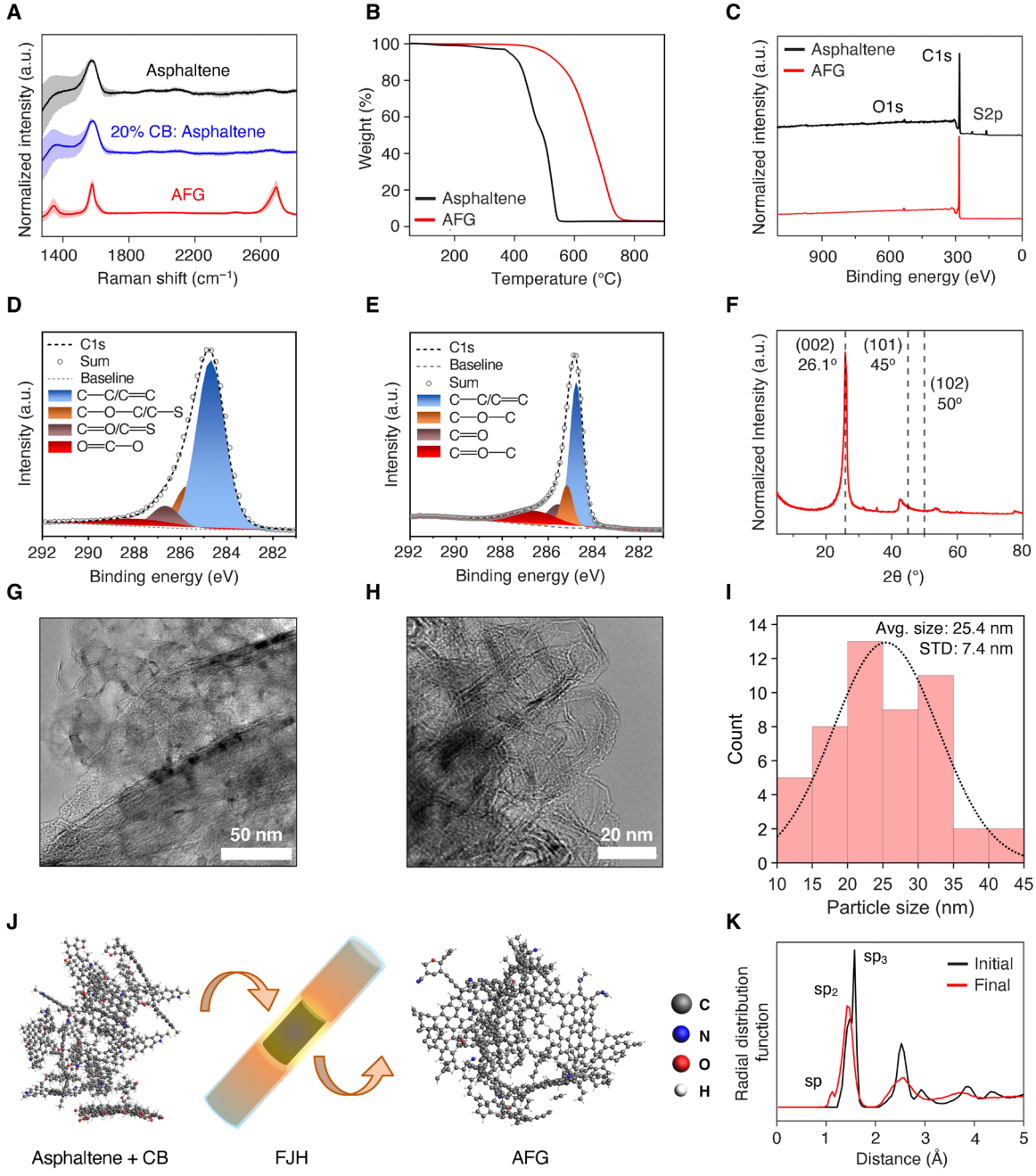

Fig. 2. Physicochemical characterization of AFG and atomistic simulation of the conversion process. (**A**) Average Raman spectra of asphaltene, asphaltene and 20% CB mixture, and AFG using 532-nm excitation wavelength with SD shown by shaded regions ($N = 100$). (**B**) TGA of asphaltene and AFG conducted in the air with a ramp rate of 10°C min^{-1}. (**C**) XPS survey spectral comparison of asphaltene and AFG. XPS high-resolution C1s spectra of (**D**) asphaltene and (**E**) AFG. (**F**) XRD spectra of AFG. (**G** and **H**) TEM images of primary flakes of AFG. (**I**) Lateral size distribution obtained by TEM image analysis techniques of the Feret diameters ($N = 100$). (**J**) Molecular dynamics simulation of the conversion of asphaltene to AFG via FJH. (**K**) Temporal evolution of the radial distribution function during the simulation.

12%. For effective mechanical reinforcement in the polymer-AFG composites, the mechanical stress applied to the composite must be transferred to the reinforcement via the polymer matrix. Uniform dispersion of AFGs into the polymer matrix resulted in improvements in mechanical properties (*29*, *30*). This is because the increased surface area of the nanoparticles improves their interfacial adhesion with the matrix, which can facilitate stress transfer between the matrix and the nanoparticles. Conversely, higher loading percentages of AFG reduce the tensile strength and Young's modulus compared to neat epoxy. This is possibly due to poor, irregular dispersion of the AFG into the matrix at higher loading, with the formation of large graphite-like aggregates that act as macroscopic defects in the material (*31*). The agglomeration may have resulted in weaker interfacial adhesion, and hence, the stress transfer between matrix and reinforcement is insufficient, leading to the reduction in strength and modulus (*32*). Figure 3F compares the toughness, measured as the

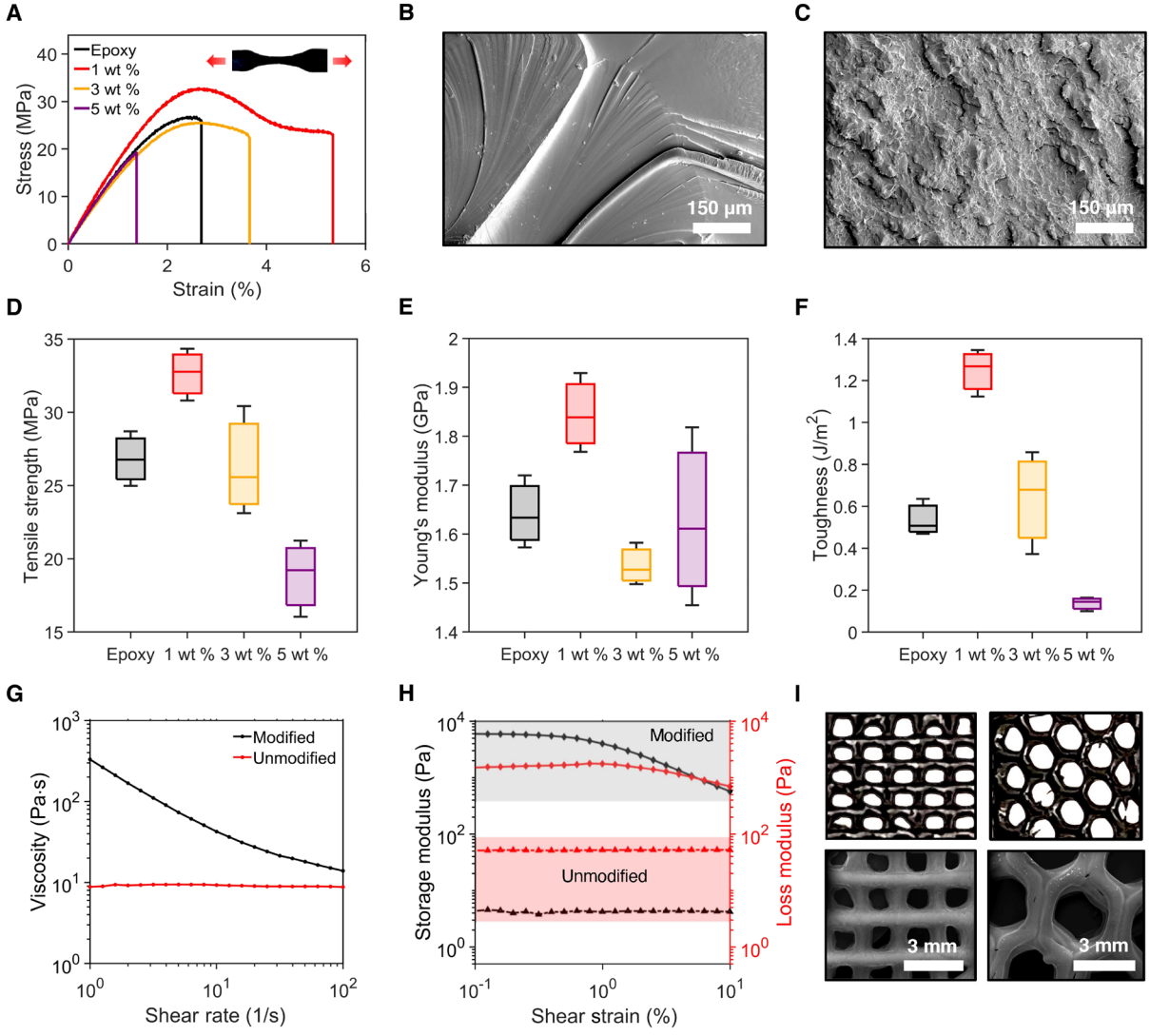

Fig. 3. Mechanical properties and 3D printability of epoxy-AFG nanocomposite. (**A**) Tensile stress-strain plots of the epoxy-AFG nanocomposites with varying wt % loading of AFG. Inset shows a fabricated dog-bone structure of the epoxy-AFG nanocomposites before tensile test. Fracture surface analysis of (**B**) neat epoxy and (**C**) epoxy-AFG nanocomposites with 1 wt % AFG loading under an SEM. Comparison of (**D**) tensile strength, (**E**) Young's modulus, and (**F**) toughness of epoxy-AFG nanocomposites with varying wt % loading of AFG. (**G**) Apparent viscosity as a function of shear rate for unmodified and modified epoxy-AFG nanocomposite ink. (**H**) Storage and loss modulus of unmodified and modified epoxy-AFG nanocomposite ink as a function of oscillation strain. (**I**) Photographs and SEM images of 3D-printed architected structures (rectangular, left; honeycomb, right) using the modified epoxy-AFG nanocomposite ink.

area under the stress-strain graph (Fig. 3A), of neat epoxy to that of the nanocomposite samples. Similarly, the toughness increased with the addition of 1 wt % AFG, while higher loading percentages had a negative effect due to reduced strength and modulus.

Fracture surface morphology of the samples was analyzed using an SEM to understand the mechanisms of these variations in mechanical properties (Fig. 3, B and C, and fig. S7). The fracture surface of the neat epoxy sample is very smooth with continuous river lines, showing uninterrupted crack propagation (Fig. 3B). This indicates the well-documented shear band propagation in cross-linked epoxies, where a single shear band can traverse the entire sample and cause failure at small strains (*29*). Conversely, the fracture surface of the 1 wt % sample (Fig. 3C) shows high roughness, suggesting large numbers of shear band formations and crack deflections throughout the sample (*33*). Thus, the extrinsic toughness of the 1 wt % AFG nanocomposite was improved by locally arresting shear bands before they could cavitate and become cracks. This stimulated multiple shear band development, which could relieve high local stresses. However, with higher loading percentages, the adverse effect of poor dispersion and agglomeration offsets the impact of these toughening mechanisms. Thus, 1 wt % AFG nanocomposite gives optimum mechanical properties, owing to its good dispersion and extrinsic toughening mechanisms, making it an effective reinforcement for structural composites.

Next, instead of mold casting, we evaluated the feasibility of fabricating epoxy-AFG nanocomposites using advanced manufacturing techniques, such as AM. AM, also known as three-dimensional (3D) printing, is considered a new industrial revolution because of its

ability to autonomously produce macroscopically complex structures with controlled microstructures and properties (*34*, *35*). Among the various AM techniques, direct ink writing (DIW) has emerged as one of the most versatile AM methods that can develop high-performance 3D structures by dispensing high-viscosity materials through a nozzle or orifice in a layer-by-layer fashion on a computer-controlled translation stage, thereby eliminating the need for any mold or template (*36*, *37*). Facilitating the 3D printing of epoxy-AFG nanocomposites through DIW has the potential to further extend the applications of AFG and thus broaden the valorization of asphaltene. Here, we investigated the DIW printability of the epoxy-AFG nanocomposite to develop architected 3D structures. One of the main challenges of DIW is to design and formulate viscoelastic inks that can easily flow through a micronozzle under shear and quickly recover upon deposition. Therefore, the ink needs to demonstrate a non–Newtonian, or more specifically, a shear-thinning behavior while possessing sufficiently high storage modulus to maintain the printed filamentary shape (*37*). The ink also needs to exhibit yield stress behavior such that it requires a certain amount of stress to be applied before the fluid begins to flow. In our investigation, the rheology test revealed that the pristine nanocomposite ink (1 wt % AFG loading) behaves as a Newtonian fluid and lacks the necessary rheological response required for DIW (Fig. 3G). Furthermore, the loss modulus (G'') of the ink is greater than the storage modulus (G') at low shear rates (Fig. 3H). This indicates that after printing, the material will not be able to maintain the filamentary shape and/or printed structure. Ideally, there should be a crossover point between the storage and loss modulus as a function of shear rate so that during extrusion, when the force is applied (high shear rates), the loss modulus is higher, and the ink acts more fluid-like, while after printing when the applied force is removed (low/no shear rates), the storage modulus is higher, and the ink acts as a solid retaining the extruded filamentary shape. To attain printability, the inks were, therefore, modified by adding a common thixotropic agent (fumed silica) (*38*). The ink formulation was optimized by adding the minimum amount of fumed silica (7.5 wt %) to obtain highly shear-thinning (Fig. 3G) and shear-yielding (Fig. 3H) behavior, which is ideal for smooth flow during printing without clogging the micronozzle. The viscoelastic behavior of the ink also improved. G' at low strain for the modified epoxy-AFG ink is one order of magnitude greater than G'', required for retaining the shape upon extrusion. Moreover, the crossover point for the modified epoxy-AFG nanocomposite ink occurs at low enough strains to enable printing using typical low extrusion forces akin to commercial DIW printers (Fig. 3H). After the rheology of the ink was optimized, modified epoxy-AFG nanocomposites having complex architectures, such as rectilinear and honeycomb structures, were 3D-printed (Fig. 3I and fig. S8). This shows that epoxy-AFG nanocomposites can be 3D-printed into complex, lightweight, and cellular architectures, which can have applications in several structural and engineering applications.

Thermal properties

Limited thermal properties of polymers, such as the inability to effectively dissipate heat, which is characteristic of low thermal conductivity, lessen their potential in many engineering applications (*39*). If a polymer can be engineered with high thermal dissipation ability, polymeric heat spreaders and heat exchangers can be manufactured with attractive features, including structural compactness, lightweight, ease of processing, and low cost, which could find many applications in electronics, water, and energy industry (*40*). Thus, enhancing the thermal properties of polymers and polymer composites is of great interest. Adding high thermally conductive fillers into polymers is one of the most efficient ways to improve the thermal properties of polymers (*41*). We, therefore, investigated the thermal properties of the epoxy-AFG nanocomposites using a thermal infrared (IR) camera, while a white supercontinuum laser was held incident on the samples for light-induced heating. As observed from the thermal mapping images (Fig. 4A), the induced heat for neat epoxy is concentrated in a smaller region compared to the nanocomposites, indicating better heat transfer/dissipation within the latter. To compare the thermal behavior of the nanocomposites to that of neat epoxy, the single-line temperature profiles were extracted from temperature mapping captured by the IR camera and analyzed (Fig. 4B). When illuminated with a laser of the same power, the line profile of neat epoxy showed higher peak temperature but smaller FWHM than those of the nanocomposites. The relatively low surface temperature of the nanocomposites indicates an improved heat transfer rate, thereby homogenizing the heat generated by the laser. To observe the time-dependent heat dissipation behavior, temporal changes in the maximum surface temperature are also recorded (Fig. 4C), which shows better performance for the nanocomposites.

To determine the thermal conductivity of the samples, the single-line temperature profile extracted from temperature mapping captured by the IR camera was compared to a finite element simulation of laser heating (Fig. 4D) in the same region (*42*). The simulation details can be found in the Supplementary Materials. A comparison of the temperature distribution along the heat source in the simulation with the experimental single-line temperature profile provides the thermal conductivity of the sample. As shown in Fig. 4E, the temperature profiles are in good agreement between experiment and simulation, yielding the thermal conductivity of neat epoxy samples to be 0.18 W/(m.K), which is within the range reported for epoxy polymer (*43*). Once the best fit was obtained for neat epoxy, we iterated the simulation with varying thermal conductivity values until the best fit was obtained for all the nanocomposites with different AFG loading (fig. S9). Note that the peak temperature is dominated mainly by sample thermal conductivity. Therefore, with increasing AFG loading, the thermal conductivity of the nanocomposites increased from 0.18 W/mK for neat epoxy to 0.46 W/mK for the nanocomposites with 5 wt % AFG (Fig. 4F), which corresponds to an improvement of ~155% in the thermal conductivity values. The improvement in the thermal properties observed for AFG was comparable to the addition of similar wt % of other carbon nanomaterials such as carbon nanotubes (CNTs) (*44*) and graphene nanoplatelets (*45*) (table S4). Such improvement is due to the improved nanofiller interconnectivity at higher loading of AFG and good interfacial interaction between the polymer and the AFG (*40*). As a result, AFG can enhance the thermal behavior of the nanocomposites by effectively transferring the thermal energy from the matrix to the nanofillers and vice versa. Furthermore, it is evident that with increasing AFG concentration, the heat transfer/dissipation and thermal conductivity of the nanocomposites improved significantly, suggesting substantial improvement in the matrix-filler interfacial thermal conductance. As the AFG concentration increases, a more densely constructed and interconnected 3D network of fillers is formed within the matrix (Fig. 4G), which facilitates better heat transfer, resulting in improved thermal properties of the nanocomposites (*31*).

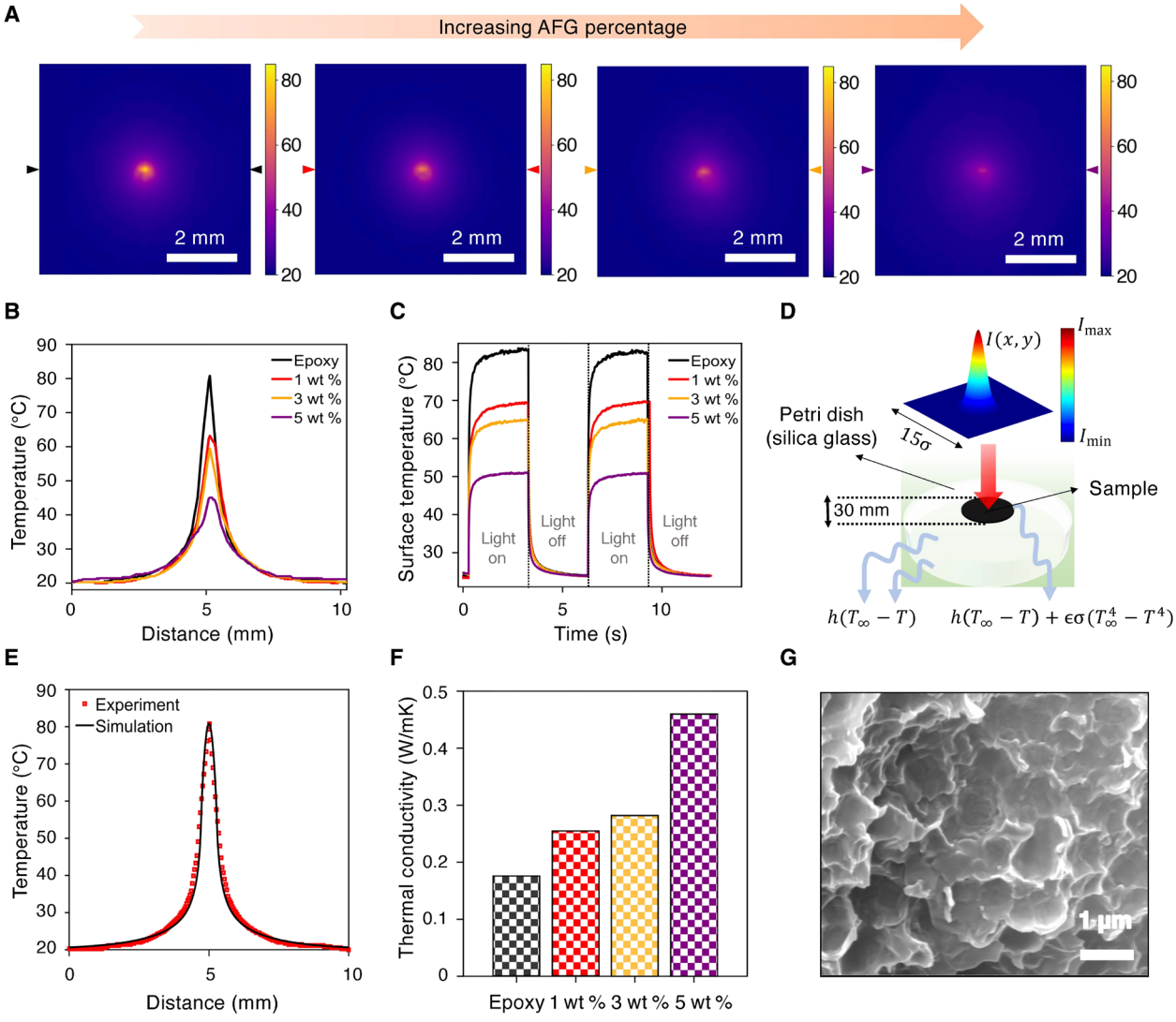

Fig. 4. Thermal properties of epoxy-AFG nanocomposites. (**A**) Temperature mapping of epoxy-AFG nanocomposites with increasing wt % of AFG (left to right: 0, 1, 3, and 5 wt %) using IR camera under 45-mW laser illumination in air. (**B**) Comparison of surface temperature line profile obtained from the thermal IR mapping [shown in (A)] along the direction marked with arrows for epoxy-AFG nanocomposites with varying wt % of AFG. (**C**) Comparison of temporal heat dissipation behavior of epoxy-AFG nanocomposites with varying wt % of AFG. (**D**) Geometry and materials used in the thermal simulation. The dissipation in the sample depends on the spatial shape of the incident laser beam. Considered Gaussian laser shape, which determines the input heat source of the thermal model, is shown on top. (**E**) Comparison between experimental and computational temperature profiles in the same region of the epoxy sample. (**F**) Surface morphology, under an SEM, reveals a densely constructed and interconnected AFG network in 5 wt % epoxy-AFG nanocomposites. (**G**) Comparison of the calculated thermal conductivity of the epoxy-AFG nanocomposites with varying wt % of AFG.

Corrosion resistance behavior

Corrosion plays a predominant role in almost all the major industries, and for a long time, polymeric coatings have been applied as a corrosion protective layer to the base material (*46*). However, to work effectively, these coatings often require expensive fillers at a higher loading level (~60% v/v) (*47*). Therefore, we investigated the use of AFG as a high-performance nanofiller to improve the corrosion resistance of commercially available epoxy coatings in simulated saline/marine environments. We use mild steel (MS) as a technologically relevant metal in our studies, which was coated with a thin layer of epoxy-AFG nanocomposite coating (epoxy-AFG/MS) with 10 wt % of AFG loading. In this case, 10 wt % was chosen since improving the functional properties of the neat matrix typically requires higher wt % of nano-reinforcement loading. We also applied a thin coating of epoxy resin (without AFG) on MS (epoxy/MS) and tested its corrosion resistance performance. As expected, the bare MS experienced a high degree of corrosion compared to the coated substrates after 6 hours of exposure to the test conditions, as shown in the optical images (Fig. 5A). The epoxy/MS developed a rough brown surface (indicating rust), while the epoxy-AFG/MS was blemished only slightly with the corrosion deposits (Fig. 5B). The superior corrosion resistance of epoxy-AFG nanocomposite coatings was quantitatively established using the potentiodynamic polarization (PDP) tests (Fig. 5C) and electrochemical impedance spectroscopy (EIS) analysis (Fig. 5D). The results from the PDP tests corroborate the outstanding ability of AFG to resist the corrosive effects of aggressive

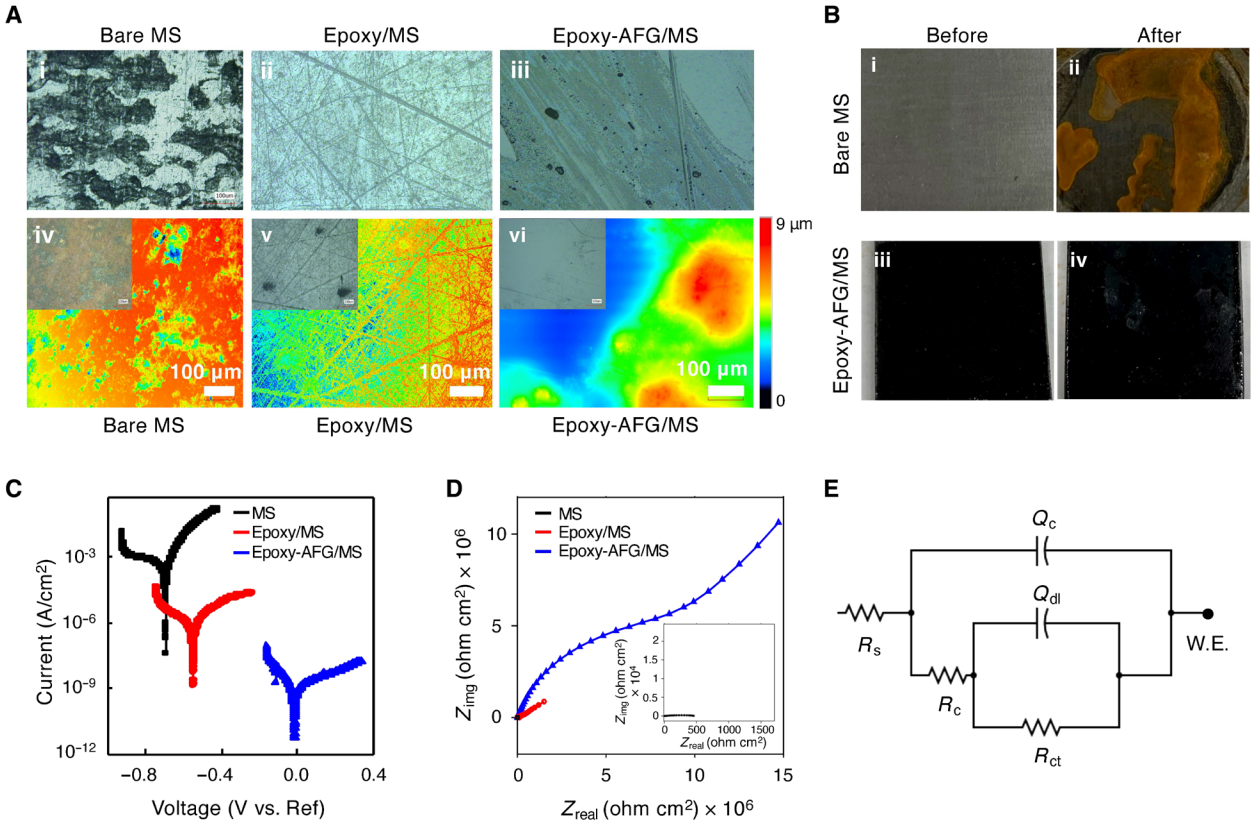

Fig. 5. Corrosion resistance performance of epoxy-AFG nanocomposite coating. The performance of the nanocomposite coating was compared with bare MS and neat epoxy coating, exposed to 3.5% NaCl. The thickness of the coatings was roughly 100 to 200 µm. (**A**) (i, ii, and iii) Optical images of MS, epoxy/MS, and epoxy-AFG/MS before exposure to a corrosive environment; (iv, v, and vi) optical images of MS, epoxy/MS, and epoxy-AFG/MS that are exposed to 3.5% NaCl solution showing corrosion deposits (rust) on mild steel. (**B**) Photographs of MS and epoxy-AFG/MS before and after exposure to 3.5% NaCl for 6 hours. (**C**) PDP plots for MS, epoxy-MS, and epoxy-AFG/MS in a potential range of ±250 mV from open-circuit voltage. (**D**) EIS plots for MS (inset), epoxy-MS, and epoxy-AFG/MS carried out using a sinusoidal AC potential of 10 mV and in the frequency range of 0.01×10^5 Hz. (**E**) Electrical equivalent circuit (EEC) used to fit the EIS plot consisted of two pairs of resistance (R) and capacitance elements connected in parallel. The first RC circuit consists of coating resistance (R_c) and a constant phase element to model coating capacitance (Q_c). The second RC circuit consists of charge transfer resistance (R_{ct}) and constant phase element.

chloride species. The open-circuit potential (OCP) for epoxy-AFG/MS (90 mV versus Ag/AgCl) was nobler (more positive) compared to epoxy/MS (−313 mV versus Ag/AgCl) and bare MS (−615 mV versus Ag/AgCl). This result suggests the ability of epoxy-AFG nanocomposite coatings to reduce the susceptibility of MS surfaces to corrosion.

The nobler corrosion potentials (E_{corr}) for epoxy-AFG/MS (−13.3 mV) compared to epoxy/MS (−544 mV) and bare MS (−690 mV) can also be observed from the Tafel plots (Fig. 5C). On the basis of the Tafel analysis, the corrosion rates for epoxy-AFG/MS [8.06×10^{-4} milli-inches/year (mpy)] were five orders and four orders of magnitude lower compared to bare MS (98.46 mpy) and epoxy/MS (1.23 mpy), respectively. The current densities for epoxy-AFG /MS (1.74×10^{-9}) were one order and three orders of magnitude higher compared to epoxy/MS and bare MS, respectively (table S5).

We used EIS as a nonintrusive tool to quantify the electrical parameters not extractable from the Tafel analysis. The EIS test results corroborated the outstanding barrier properties of the epoxy-AFG coating (Fig. 5D). By comparing the magnitudes of the Nyquist arcs, it can be observed that the epoxy-AFG/MS offers several orders of higher electrochemical polarization resistance compared to epoxy/MS. To quantify the corrosion resistance performance of the nanocomposite coating, the EIS data (Fig. 5D) from the Nyquist plots were analyzed using the electrical equivalent circuit (EEC) (Fig. 5E) fitting method. In this case, the epoxy-AFG coating was also found to offer superior corrosion resistance (table S6). Specifically, the charge transfer resistance, R_{ct}, for epoxy-AFG/MS (~9.83×10^6 Ω·cm^2) was three orders of magnitude higher than epoxy/MS (~1.03×10^3 Ω·cm^2) and six orders higher than bare MS (~530.7 Ω·cm^2). Furthermore, the coating capacitance (Q_c) of epoxy-AFG/MS (153.3×10^{-9} µF/cm^2) was six orders of magnitude less than bare MS (2.93×10^{-3} µF/cm^2), which corroborates the superior barrier properties of epoxy-AFG/MS. These results demonstrate that AFG has the potential to enhance the corrosion resistance of polymer coatings by forming an effective barrier coating against intercalating corrosive species into the epoxy coating. Furthermore, the use of AFG in corrosion-resistant coating bears add-on benefits as it involves inexpensive raw materials (asphaltene) and minimal processing conditions.

Environmental impacts and cost analysis

To quantify the environmental impacts of AFG synthesis, we performed a gate-to-gate LCA and compared it with the existing use of asphaltene as an energy-dense medium (i.e., fuel) (Fig. 6A and table S7)

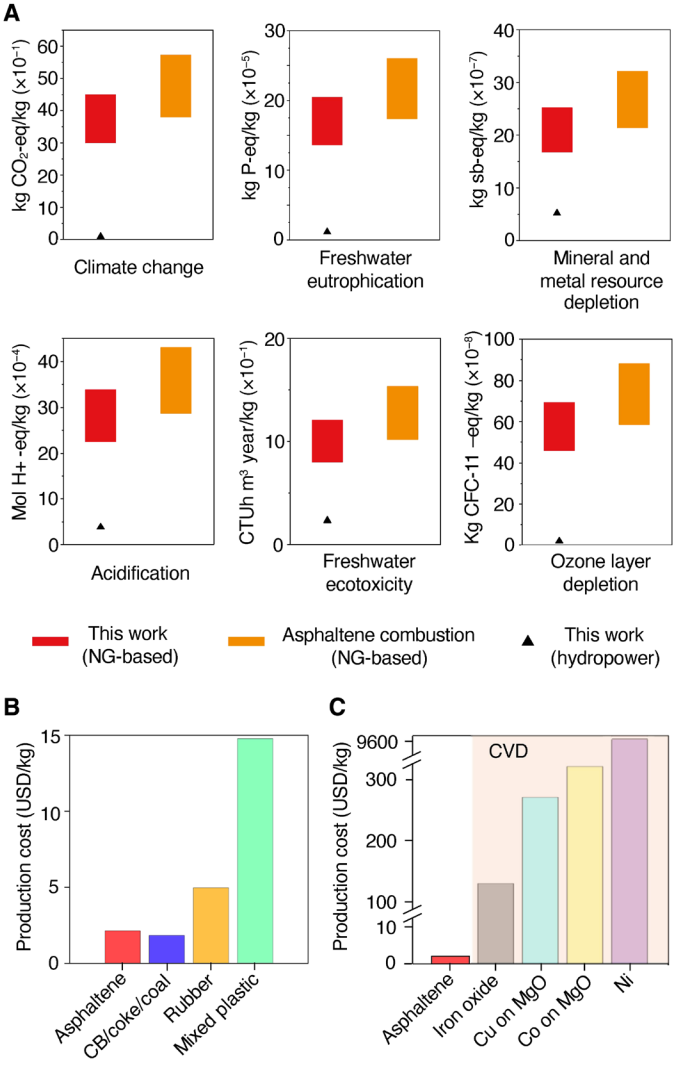

Fig. 6. Environmental impact and cost analysis of AFG. (**A**) Gate-to-gate life cycle assessment of FJH of asphaltene as compared to asphaltene combustion used as an energy-dense carrier (i.e., fuel) in practice. Two electricity generation scenarios have been considered: natural gas and hydropower based, which drive the results of six midpoint impact categories—climate change, freshwater eutrophication, minerals and metal resource depletion, acidification, freshwater ecotoxicity, and ozone layer depletion (*48*). Techno-economic analysis showing the comparison of production cost of AFG with respect to (**B**) various FJH precursors and (**C**) graphene synthesized by CVD techniques. The shaded region contains the production cost of graphene synthesized by various CVD methods.

(*10*–*12*). For our work, the associated energy input for the optimized FJH process for converting asphaltene to AFG was calculated (details available in the Supplementary Materials and table S8). The maximum energy content of asphaltene as fuel during combustion was determined by calculating a higher heating value (or gross calorific value) using Dulong's formula (*48*). In both cases, the functional unit was maintained as 1 kg of asphaltene, and following International Life Cycle Data (ILCD) system guidelines, six midpoint indicators were analyzed, namely, climate change, freshwater eutrophication, minerals and metal resource depletion, acidification, freshwater ecotoxicity, and ozone layer depletion. To accommodate the uncertainties associated with scale-up, theoretical heat content calculation, and emission factors, a 20% error range was assigned to the base value of each impact category.

For the asphaltene combustion route, the overall energy content or energy required for oxidation is higher than the equivalent electricity required for the AFG conversion route. This relatively higher energy for the combustion route originates from the higher carbon composition (~80%) of asphaltene, which, upon exothermal reaction with oxygen, will generate increased emissions. Elements such as sulfur and other noncombustible elements in asphaltene further contribute to overall emissions. Concurrently, across all impact categories, the overall environmental impacts of asphaltene to AFG conversion are lower than the combustion route due to lower energy requirements from the single-step and energy-efficient FJH process. Being a gate-to-gate analysis, the results of the impact categories are either driven by electricity input (for AFG route) or energy equivalent (combustion route). For the AFG route, the final pulse of 370 V determines the FJH via complete discharge (*18*, *50*) and hence contributes the most toward energy consumption (~47%) (table S8). Thus, further optimization of pulsed voltages used for pretreatment and discharge would significantly lower the environmental impacts of the AFG route.

The electricity generation technology for this analysis has been assumed to be a natural gas-based energy carrier without carbon capture and storage, as described in table S9 (*49*). Thus, to estimate the effect of renewable energy, a hydropower-based scenario (*49*) (table S9) has been depicted for AFG synthesis, and the results are shown as "triangles" in Fig. 6A. Comparing the six impact categories, hydropower-based AFG has the lowest environmental impact concluding the importance of renewable energy once looked through the lens of environmental benefits.

Last, a technoeconomic analysis of the FJH process for the conversion of asphaltene to AFG has been conducted. The AFG production cost shown in Fig. 6B is calculated on the basis of the cost of precursor (plastic waste, inexpensive carbon sources, CB, rubber, and asphaltenes) and electrical energy used for FJH methods (table S10). The yield of asphaltene to the AFG process is reported at 45%, and the electrical energy requirement for conversion is ~20.55 kJ/g (Supplementary Materials). The cost of electricity is considered at USD 0.05/kilowatt-hour (kWh), and the cost of asphaltenes is taken as USD 0.52/kg (*10*). Because of the relatively good yield and lower cost of asphaltene, the production cost of AFG becomes 2.15 USD/kg. In addition to asphaltene, the cost of FG from inexpensive carbon sources (CB/coke/coal) is also low. This is due to the high yield and low cost of the precursors. However, other carbonaceous sources, such as plastic waste and rubber, have either higher precursor costs or lower yields and, therefore, higher production costs (*18*, *22*, *50*). A detailed economic comparison of AFG with other FJH feedstocks such as coke/coal, rubber, and mixed plastic can be found in the Supplementary Materials (fig. S10).

We also compared the production cost of AFG, as shown in Fig. 6C, with graphene synthesized by conventional synthesis techniques such as CVD (*51*, *52*). Although it is not a fair comparison since CVD grows a monolayer or few layers of graphene over large areas, it was done just to assess the economic feasibility of the FJH process, especially considering the bulk-scale synthesis of AFG from asphaltenes. The cost of CVD graphene is determined by the price of the catalyst and the amount of catalyst needed to produce graphene for each synthesis method (*53*, *54*). As seen in Fig. 6B, the cost of AFG was found to be significantly low compared to the CVD-grown graphene.

DISCUSSION

While the world transitions to renewable fuels and energy sources, the reality is that petroleum-based energy sources will still be in demand in the foreseeable future. Thus, the challenge lies in managing the global primary energy resources sustainably in ways to reduce, if not eliminate, emissions and simultaneously facilitate valorization of low-value by-products. In an effort to reconcile the environmental imperative, we have developed a strategy to transform asphaltenes into a high-value carbon allotrope, graphene, via FJH. A series of physicochemical characterization techniques and theoretical modeling has confirmed the successful conversion of asphaltene to graphene. Following the conversion process, asphaltene-derived graphene was used as a reinforcement in a value chain of high-performance nanocomposites, which can be used in various applications ranging from structural and thermal to anticorrosion coating. Then, we show that environmental degradation and economic expenses associated with the existing processing of asphaltene can be sequestered via FJH of asphaltene. Hence, the comprehensive technological scheme presented here can contribute to the global economy and reduce emissions during the energy transition in the near future.

MATERIALS AND METHODS

Materials

Asphaltene powders (Alberta oil sands asphaltenes) were received from InnoTech Alberta and used as received. CB (BP-2000) was purchased from Cabot Corporation and added to asphaltene at a ratio of 1:4 to increase the conductivity. Before the FJH process, the blend of 20% CB:asphaltene was ball-milled at 400 rpm for 2 hours to ensure homogeneous mixing of the blend.

FJH process

The ball-milled CB:asphaltene was placed inside a quartz tube between two copper electrodes and subjected to a variably FJH pulse with duty cycles at 10% 1 s, 20% 0.5 s, and 50% 5 s and a frequency of 1000 Hz. Four pulses were used at 185, 250, 250, and 370 V, in order, resulting in AFG. A submillimeter space between the electrodes and the quartz sidewall was maintained to permit outgassing upon FJH.

The synthesized AFG from a former run can be used as a conductive additive instead of CB, but a higher proportion is needed. At 20% AFG and 80% asphaltene, the resistance of a 500-mg sample in an Inner Diamater (ID) 8-mm tube is ~64 kilohms. At 50% AFG and 50% asphaltene, the resistance is reduced to ~60 ohms. AC pretreatment further decreases resistance to ~6 ohms. Two pulses at 150 and 200 V for 500 ms can then be used to convert this blend into 50-50 AFG-asphaltene FG with 67.6% process yield and 94.8% process yield.

Raman spectroscopy analysis

Raman spectra were collected with a Renishaw inVia confocal Raman microscope and a 532-nm laser. A laser power of 5 mW and a 50× objective lens were used, and samples were scanned from 1300 to 2800 cm^{-1}. Before collection, AFG samples were ground with a mortar and pestle to ensure homogeneity without the use of solvent. Large-area Raman mapping was used to assess the crystallinity and nanostructure of the graphene before analysis using a custom-written Python script using the RamPy package. Raman spectra were background-corrected and smoothed using a Savitsky-Golay filter before the quantification of graphene yield and peak ratios. Spectra with a minimum I_{2D}/I_G ratio of 0.3, a signal-to-noise ratio of >5 in the 2D band region, and a 2D band with an FWHM of <100 cm^{-1} were classified as graphene. The average Raman spectrum of AFG was obtained after collecting 100 different spectra.

Thermogravimetric analysis

All TGA thermograms were collected using AFG and asphaltene that were ground with a mortar and pestle to ensure homogeneity without the use of solvent. Alumina pans were used in a Mettler Toledo TGA/DSC 3+ system. A range of 50° to 900°C was used for data collection, with a heating rate of 10°C min^{-1}. All samples were run under an atmosphere of air.

X-ray photoelectron spectroscopy

The surface elemental compositions and chemical states of asphaltene and AFG were analyzed by XPS (PHI Quantera II with monochromated Al Kα at 1486.6 and 26-eV pass energy, 50 W, 15 kV, and 200-μm-diameter x-rays were shot on the sample). The XPS survey scan spectra in the 1100- to 0-eV binding energy range were recorded in 0.5-eV steps with a pass energy of 140 eV. High-resolution spectra were recorded in 0.1-eV steps with a pass energy of 26 eV.

X-ray diffraction

XRD was performed on AFG using a Rigaku D/Max Ultima II powder XRD in the scan range of 10° to 80° configured with CuKα radiation, a graphite monochromator, and a scintillator counter.

Transmission electron microscopy

Dilute solutions (~1 mg ml^{-1}) of AFG were sonicated (Cole-Parmer 750-watt ultrasonic processor with a cup horn) for 15 min before drop-casting onto a 200-mesh Cu grid with lacey carbon. A JEOL 2100 F field-emission gun TEM at 200 kV was used to image the sample.

Atomistic simulation

ReaxFF is a reactive force field simulation method that is a bond order–based molecular dynamics technique that considers the instantaneous interaction between atoms and molecules (*24*). The highlight of this computational method is that it allows for smooth translation between nonbonded and bonded states that help to simulate and look into the chemical reactions where bond formation and bond dissociation are involved during simulation (*25*). This is specifically helpful for the carbonization process (*26*) that we expect to see in flash graphene.

Materials that go through carbonization are difficult to simulate using reactive potentials due to competing hybridizations and long-range effects associated with π-electrons. The recently developed C/H/N/O ReaxFF (reactive) force field is able to bypass these limitations mainly since it has been trained using extensive density functional theory data (*55*). This force field has successfully been able to capture carbonization reaction mechanisms for carbon fiber and laser-induced graphene.

The simulation box with dimensions of 50 Å by 50 Å by 50 Å consisted of 10 molecules of asphaltene (fig. S5) along with a graphitic structure that represents the surface of CB (fig. S5) with an initial density of 0.2 g/cm^3. The simulation box had periodic boundary conditions on all sides. An NVT ensemble (number of molecules, volume, and the temperature kept constant) was used to simulate the system using a 0.25-fs time step; the temperature was ramped up in steps from 300 to 3000 K at 200 K/ps and kept there for ~0.62 ns.

Mechanical testing

All uniaxial in-plane tensile tests were conducted at room temperature using an MTS 858 servohydraulic machine in accordance with ASTM d638 Type V scaled to a length of ~6 cm and a width of ~9.5 cm. The loading rate was 1 mm min^{-1}, and the span length was fixed for each sample at 30 mm. The test was performed using a 5-kN load cell, and the data were recorded until the specimen fractured. At least three specimens were tested for each formulation category to ensure the consistency of the data.

Scanning electron microscopy

Morphology and fracture surfaces were observed using two field-emission SEM (FEI Quanta 400 and FEI Helios SEM/FIB) with 20-kV accelerating voltage. The surfaces were coated with a thin layer of gold (~10 nm) using a sputter coater to prevent charging.

Formulation of epoxy-AFG nanocomposite

Epoxy-AFG nanocomposite ink was prepared by dispersing AFGs into a 3:1 (resin/curing agent) formula of epoxy resin (Epon 826 and Jeffamine D230, Sigma Aldrich). AFGs were ground using a mortar and pestle, and the ground AFGs were added to an equal amount (by weight as that of epoxy resin) of acetone (dispersion medium). Next, the acetone containing AFG was bath- and probe-sonicated for 30 min each. In the meantime, the epoxy resin was heated to 100°C to reduce the viscosity for 10 min. After that, epoxy resin was added to the mixture and was bath- and probe-sonicated for 30 min each. The mixture was then put on a hot plate at 70°C for a few hours, followed by vacuum desiccation for ~6 hours, which ensured almost complete removal of acetone. Next, Jeffamine (curing agent) was added at a weight ratio of 3:1 (resin/curing agent) and mixed with a planetary centrifugal mixer (THINKY MIXER ARE 310) at 2000 rpm for 4 min. Last, the mixture was desiccated for 5 to 10 min.

Mold casting

To cast the epoxy-AFG nanocomposite ink that was prepared following the fabrication section above, a stainless steel dog-bone mold (following ASTM d638) was greased to prevent adhesion of the nanocomposite to the mold. The epoxy-AFG nanocomposite ink was cast onto the greased mold. To prevent void expansion during curing, the ink was set for 48 hours at room temperature, followed by a second curing step at 130°C for 1 hour. The cured specimens were removed from the mold while still hot to prevent fracture and the introduction of residual stresses. After curing, the samples were polished to remove surface disparities.

3D printing of epoxy-AFG nanocomposites

Epoxy-AFG nanocomposite ink for 3D printing was prepared following the exact same procedure mentioned in the "Formulation of epoxy-AFG nanocomposite" section, except that 7.5 wt % fumed silica (Sigma Aldrich, S5130-100G) was added and mixed using the THINKY mixer before the Jeffamine addition step. The prepared ink was loaded into a 30-ml Luer-lock syringe and centrifuged to remove air bubbles. Smooth-flow tapered tips (Nordson EFD) were used to further ensure that any remaining air bubbles do not clog the tip during printing, which would cause nonuniform printing. Using a high-resolution 3D printer (Hyrel3D Engine HR), epoxy-AFG inks were extruded at room temperature onto silicone mats fixed to the 3D printing build plate. Slic3r software was used to generate the G code script for 3D printing based on the designed geometry and other programmed parameters, including extrusion width, printing speed, and layer height, to determine the printing path. The 3D-printed samples were cured following the same protocol as the mold cast specimen. After 48 hours at room temperature, the 3D-printed structures were heated to 130°C for 1 hour.

Rheological characterization

Rheological properties of inks were measured using ARES G2 Rheometer using a cone and plate geometry (25-mm diameter with a lower cone angle of 0.1 rad and a gap of 0.05 mm between the plates). Flow and viscosity curves were obtained with a flow ramp experiment where the strain rate was logarithmically increased from 0.1 to 100 s^{-1}. Oscillatory amplitude sweeps were performed at an angular frequency of 1 Hz with the strain from 0.01 to 10%.

Thermal measurement (IR camera)

In situ surface temperatures were recorded with a thermal IR camera (FLIR, A615) during the measurements. White light from a supercontinuum laser (Fianium, WL-SC-400-8; 400 to 900 nm, 4 ps, 80 MHz) was applied for light-induced heating, and a lens was applied to focus the beam such that the spot size of the illumination on the sample is ~1.0 mm^2. A neutral density filter (Thorlabs, NDC-100C-4M) was applied to adjust the total power of illumination to 25 mW. Direct illumination of the thermal camera with our light source did not cause any observable increase in temperature, indicating that the illumination source has no mid-IR (2 to 10 μm) photons. Therefore, the measured temperature increases during the experiments resulted only from photothermal heating effects rather than the scattering of the incident light.

For each sample, a glass petri dish with a diameter of 93.0 mm was flipped over on the optic table to hold the sample, which was placed at the center of the dish. The incident light is aligned to be perpendicular to and centered at the top surface of the sample, and the thermal camera image was taken at 25° away from the incident light. The focus of the thermal camera is optimized before measuring each sample and kept consistent throughout the measurement with respect to that sample. However, for different samples, the focus may be different depending on the shape and geometry of the sample. The thermal images of the illuminated samples were then collected, and the temperature line profile along different directions on the sample surface was extracted for comparison.

The time-dependent heat dissipation measurement was performed by monitoring the time profile of the highest surface temperature after illumination and blocking of the beam. The light is on for 60 s before it is blocked for dissipation measurements, which lasts for another 60 s. Two rounds of on-off experiments were performed for each sample.

Finite element simulation of laser heating

Thermal simulations have been performed using commercial software, COMSOL Multiphysics. The simulation domain consists of a disk-like 3D geometry (diameter, 30 mm; thickness, 1 mm) for the samples atop an inverted petri dish (diameter, 93 mm; thickness, 2 mm; height, 15 mm) made of silica glass for all the simulations (Fig. 4D). The model solves in stationary mode for the temperature variable, T, the thermal transport equation

$$\nabla \cdot \boldsymbol{q} = Q \text{ with } \mathbf{q} = -k\nabla T \quad (1)$$

where k represents the thermal conductivity of each material included in the model. The heat source (Q) is applied on the surface of the sample and follows a typical Gaussian shape form (Fig. 4D)

$$Q = Q(x,y) = I(x,y) = \alpha \frac{P_{in}}{(1\ m)^2} \frac{1}{2\pi\sigma^2} e^{-\frac{x^2+y^2}{2\sigma^2}} \quad (2)$$

where $\alpha = 0.9$,the assumed fraction of light is converted into heat by the sample, $\sigma = 0.282$ mm describes the beam size, and $P_{in} = 25$ mW. All the surfaces were subjected to convective ($h = 15$ W/m^{2}K) and radiative ($\epsilon = 1$) heat transfer to an ambient atmosphere ($T_\infty = 20$°C).

Electrochemical corrosion test

DC methods of electrochemical characterization were based on PDP. EIS was used to noninvasively study the electrochemical response of the coatings. The electrochemical testing was carried out using a Gamy Reference 600 with Ag/AgCl and graphite plate as reference and counter electrode, respectively. The working electrode (WE) was based on bare and coated forms of MS samples (1 cm^2). They include bare MS, epoxy/MS, and AFG/MS. The electrolyte was based on 3.5% NaCl (0.6 M). The electrochemical measurements were obtained only after achieving a steady-state OCP value. The PDP tests were carried out in a potential range of ±250 mV (versus OCP) at a scan rate of 0.2 mV/s (*47*). The corrosion current (i_{corr}) from the potentiodynamic tests (Tafel plots) was deduced from the linear portion of the anodic and cathodic branches that intersect at the corrosion potential (E_{corr}) (*56*). The corrosion rate was measured in milli-inches/year using Eq. 3 and with corrosion rate constant, $K = 1.288 \times 10^5$ milli-inches, an equivalent weight (EW) of 25.12 g, and a density (ρ) of 7.9 g/cm^3 of MS with an exposed area (A) of 1 cm^2

$$\text{Corrosion rate (mpy)} = \frac{K\, i_{corr}(\text{EW})}{\rho A} \quad (3)$$

All the EIS tests were carried out at the OCP conditions using an AC signal with an amplitude of ±10 mV. A range of 10,000 to 0.01 Hz range was selected to obtain the corresponding EIS spectra. The corrosion resistance of the coating was determined using the value of the real impedance (Z_{real}), which can be obtained when the imaginary impedance value ($Z_{imaginary}$) tends to zero at the lowest frequency (0.01 Hz). The magnitude value for the impedance was calculated using Eq. 4

$$Z_{mod} = \sqrt{Z_{real}^2 + Z_{imaginary}^2} \quad (4)$$

The EEC circuit for both the test cases and control was based on solution resistance (R_s), constant phase elements that represent the capacitances of the coating (Q_c), and the electrochemical double layer between the MS/electrolyte (Q_{dl}). The circuit also includes elements for considering the charge transfer resistance (R_{ct}) to Faradaic reactions influencing corrosion at the steel/electrolyte interface, barrier-coating resistance (R_c), and solution resistance (R_S).

Methodology for LCA

The LCA analysis was conducted following the ISO standard series 14040, and environmental impact categories were assessed on the basis of energetic input for a gate-to-gate system boundary. To avoid multifunctionality problems within the boundary, a functional unit of constant mass (1 kg) of asphaltene feedstock was considered that allowed to compare AFG and asphaltene combustion routes in terms of environmental impacts and energy requirement. The system boundaries include the phases of pulsed AFG synthesis and asphaltene combustion as fuel only.

The life cycle inventory consists of the overall electricity input required for the AFG route as well as the equivalent energy required for asphaltene combustion. The required inventory data for energy input were acquired from laboratory-scale experimental conditions, literature, and the Ecoinvent database (*57*). The six impact categories were selected on the basis of the ILCD system guidelines for the midpoint approach. The selected impact categories and their key assumptions are presented in table S7.

Electricity requirement for pulsed FJH method towards AFG route

The electricity requirement of FJH can be calculated by the following equation (Eq. 5), where E is the energy per gram, V_1 and V_2 are the voltage before and after FJH, respectively, C is the capacitance of the system (0.624 F), and M is the mass of the batch (4 g)

$$E = ((V_1^2 - V_2^2) \times C)/(2 \times M) \quad (5)$$

For a typical process, four pulses are used: 185, 250, 250, and 370 V. The initial feedstock is packed into a quartz tube with an inner diameter of 16 mm and an outer diameter of 20 mm. The first three pulses (185, 250, and 250 V) are used as pretreatment to remove volatiles and noncarbon materials and typically discharge to 150, 100, and then <10 V, respectively, as the resistance of the material decreases. The final pulse of 370 V almost completely discharges as the FJH is carried out. All tons are US tons.

As such,

Pulse 1: $V_1 = 185$ V, $V_2 = 150$ V, $E = 0.91455$ kJ g^{-1} = 230.46 kWh/ton

Pulse 2: $V_1 = 250$ V, $V_2 = 100$ V, $E = 4.095$ kJ g^{-1} = 1031.92 kWh/ton

Pulse 3: $V_1 = 250$ V, $V_2 = 10$ V, $E = 4.8672$ kJ g^{-1} = 1226.51 kWh/ton

Pulse 4: $V_1 = 370$ V, $V_2 = 5$ V, $E = 10.67625$ kJ g^{-1} = 2690.37 kWh/ton

Calculation of higher heating value for asphaltene combustion

According to most literatures, asphaltene lacks a definite chemical composition or molecular weight owing to its wide distribution of polarities (*54*, *55*, *58*). To predict their molecular structure, two types of models have been proposed, which are (i) archipelago models and (ii) island models. The archipelago models assume that several aromatic clusters are connected via aliphatic chains, and the island models propose that there is a predominantly fused polycyclic aromatic hydrocarbon ring system within each asphaltene molecule with pendant aliphatic chains. Archipelago models are reported to align with experimental pyrolysis data more strictly (*55*, *56*, *59*). Sheremata *et al.* (*60*) used the Monte Carlo method to predict the structure of Athabasca asphaltenes, and the molecular weight of asphaltene was determined by vapor pressure osmometry using *o*-dichlorobenzene as the solvent. This has been reported as the first archipelago model of asphaltene yielding a quantitative molecular

formula of $C_{318}H_{395}N_6O_6S_8V$ and molecular weight of 4705 g/mol. For the combustion of asphaltene as a fuel, we have calculated the maximum energy content or higher heating value of asphaltene using this molecular structure.

Here, the elemental composition of asphaltene on a mass basis (wt %) is given by

$$\text{Carbon (C)} = \frac{\frac{(12*318)\text{g}}{\text{mol}}}{4705\frac{\text{g}}{\text{mol}}} = 0.81$$

$$\text{Hydrogen } (H_2) = \frac{\frac{(1*395)\text{g}}{\text{mol}}}{4705\frac{\text{g}}{\text{mol}}} = 0.08$$

$$\text{Oxygen } (O_2) = \frac{\frac{(16*6)\text{g}}{\text{mol}}}{4705\frac{\text{g}}{\text{mol}}} = 0.02$$

$$\text{Sulfur (S)} = \frac{\frac{(32.065*8)\text{g}}{\text{mol}}}{4705\frac{\text{g}}{\text{mol}}} = 0.054$$

Thus, we can apply Dulong's formula (Eq. 6) using the above elemental compositions to calculate a higher heating value (HHV) of asphaltene (*61*)

$$\begin{aligned}\text{HHV} &= (33,800\,\text{C} + 144,000\,(\text{H}_2 - \text{O}_2/8) + 9270\,\text{S})\ \text{kJ/kg}\\ &= (33,800*0.81 + 144,000\,(0.08 - 0.02/8) + 9270*0.054)\ \text{kJ/kg} = 39,641\ \text{kJ/kg}\\ &= 11.01\ \text{kWh/kg}\end{aligned} \quad (6)$$

SUPPLEMENTARY MATERIALS

Supplementary material for this article is available at https://science.org/doi/10.1126/sciadv.add3555

REFERENCES AND NOTES

1. P. K. Maurya, S. Mondal, V. Kumar, S. P. Singh, Roadmap to sustainable carbon-neutral energy and environment: Can we cross the barrier of biomass productivity? *Environ. Sci. Pollut. Res.* **28**, 49327–49342 (2021).
2. O. C. Mullins, A. Ballard Andrews, A. E. Pomerantz, C. Dong, J. Y. Zuo, T. Pfeiffer, A. S. Latifzai, H. Elshahawi, L. Barré, S. Larter, Impact of Asphaltene Nanoscience on Understanding Oilfield Reservoirs. Paper presented at the SPE Annual Technical Conference and Exhibition, Colorado, USA, 30 October 2011.
3. S. Tazikeh, J. Sayyad Amin, S. Zendehboudi, M. Dejam, I. Chatzis, Bi-fractal and bi-Gaussian theories to evaluate impact of polythiophene-coated Fe_3O_4 nanoparticles on asphaltene precipitation and surface topography. *Fuel* **272**, 117535 (2020).
4. J. Bartholdy, S. I. Andersen, Changes in asphaltene stability during hydrotreating. *Energy Fuels* **14**, 52–55 (2000).
5. M. Kamkar, G. Natale, A review on novel applications of asphaltenes: A valuable waste. *Fuel* **285**, 119272 (2021).
6. S. Saad, A. S. Zeraati, S. Roy, M. A. Shahriar Rahman Saadi, J. R. Radović, A. Rajeev, K. A. Miller, S. Bhattacharyya, S. R. Larter, G. Natale, U. Sundararaj, P. M. Ajayan, M. M. Rahman, M. G. Kibria, Transformation of petroleum asphaltenes to carbon fibers. *Carbon* **190**, 92–103 (2022).
7. Y. Shahebrahimi, A. Fazlali, H. Motamedi, S. Kord, A. H. Mohammadi, Effect of various isolated microbial consortiums on the biodegradation process of precipitated asphaltenes from crude oil. *ACS Omega* **5**, 3131–3143 (2020).
8. F. A. Atiku, K. D. Bartle, J. M. Jones, A. R. Lea-Langton, A. Williams, A study of the combustion chemistry of petroleum and bio-fuel oil asphaltenes. *Fuel* **182**, 517–524 (2016).
9. L. Artok, Y. Su, Y. Hirose, M. Hosokawa, S. Murata, M. Nomura, Structure and reactivity of petroleum-derived asphaltene. *Energy Fuels* **13**, 287–296 (1999).
10. J. Zhou, P. Bomben, M. Gray, B. Helfenbaum, "White paper on bitumen beyond combustion" (Alberta Innovates, 2021; https://albertainnovates.ca/app/uploads/2022/06/AI-BBC-WHITE-PAPER__WEB-1.pdf).
11. M. Alipour, V. Kurian, S. Dhir, R. Gupta, Analysis of syngas cooler fouling from asphaltene gasification. *Fuel Process. Technol.* **152**, 7–14 (2016).
12. J.-M. Zhu, J.-B. Liu, M. K. Siddiqui, W. Nazeer, Y. Liu, Fuel gas production from asphaltene and recycled polyethylene. *Petroleum Sci. Technol.* **38**, 428–431 (2020).
13. O. C. Mullins, The asphaltenes. *Annual Rev. Anal. Chem.* **4**, 393–418 (2011).
14. K. S. Lee, M. Park, S. Choi, J.-D. Kim, Preparation and characterization of N, S-codoped activated carbon-derived asphaltene used as electrode material for an electric double layer capacitor. *Colloids Surf. A Physicochem. Eng. Asp.* **529**, 107–112 (2017).
15. D. Baran, M. F. Yardim, H. Atakül, E. Ekinci, Synthesis of carbon foam with high compressive strength from an asphaltene pitch. *New Carbon Mater.* **28**, 127–132 (2013).
16. F. Qin, X. Tian, Z. Guo, W. Shen, Asphaltene-based porous carbon nanosheet as electrode for supercapacitor. *ACS Sustain. Chem. Eng.* **6**, 15708–15719 (2018).
17. F. Qin, Z. Guo, J. Wang, S. Qu, P. Zuo, W. Shen, Nitrogen-doped asphaltene-based porous carbon nanosheet for carbon dioxide capture. *Appl. Surf. Sci.* **491**, 607–615 (2019).
18. D. X. Luong, K. V. Bets, W. A. Algozeeb, M. G. Stanford, C. Kittrell, W. Chen, R. V. Salvatierra, M. Ren, E. A. McHugh, P. A. Advincula, Z. Wang, M. Bhatt, H. Guo, V. Mancevski, R. Shahsavari, B. I. Yakobson, J. M. Tour, Gram-scale bottom-up flash graphene synthesis. *Nature* **577**, 647–651 (2020).
19. A. C. Ferrari, J. C. Meyer, V. Scardaci, C. Casiraghi, M. Lazzeri, F. Mauri, S. Piscanec, D. Jiang, K. S. Novoselov, S. Roth, A. K. Geim, Raman spectrum of graphene and graphene layers. *Phys. Rev. Lett.* **97**, 187401 (2006).
20. J.-B. Wu, M.-L. Lin, X. Cong, H.-N. Liu, P.-H. Tan, Raman spectroscopy of graphene-based materials and its applications in related devices. *Chem. Soc. Rev.* **47**, 1822–1873 (2018).
21. F. Farivar, P. Lay Yap, R. U. Karunagaran, D. Losic, Thermogravimetric analysis (TGA) of graphene materials: Effect of particle size of graphene, graphene oxide and graphite on thermal parameters. *C* **7**, 41 (2021).
22. P. A. Advincula, D. X. Luong, W. Chen, S. Raghuraman, R. Shahsavari, J. M. Tour, Flash graphene from rubber waste. *Carbon* **178**, 649–656 (2021).
23. Z. Q. Li, C. J. Lu, Z. P. Xia, Y. Zhou, Z. Luo, X-ray diffraction patterns of graphite and turbostratic carbon. *Carbon* **45**, 1686–1695 (2007).
24. A. C. T. van Duin, S. Dasgupta, F. Lorant, W. A. Goddard, ReaxFF: A reactive force field for hydrocarbons. *J. Phys. Chem. A* **105**, 9396–9409 (2001).
25. T. P. Senftle, S. Hong, M. M. Islam, S. B. Kylasa, Y. Zheng, Y. K. Shin, C. Junkermeier, R. Engel-Herbert, M. J. Janik, H. M. Aktulga, T. Verstraelen, A. Grama, A. C. T. van Duin, The ReaxFF reactive force-field: Development, applications and future directions. *npj Comput Mater.* **2**, 15011 (2016).
26. A. Vashisth, M. Kowalik, J. C. Gerringer, C. Ashraf, A. C. T. van Duin, M. J. Green, ReaxFF simulations of laser-induced graphene (LIG) formation for multifunctional polymer nanocomposites. *ACS Appl. Nano Mater.* **3**, 1881–1890 (2020).
27. X. Zang, C. Jian, S. Ingersoll, H. Li, J. J. Adams, Z. Lu, N. Ferralis, J. C. Grossman, Laser-engineered heavy hydrocarbons: Old materials with new opportunities. *Sci. Adv.* **6**, eaaz5231 (2020).
28. M. M. Rahman, M. Hosur, S. Zainuddin, K. C. Jajam, H. V. Tippur, S. Jeelani, Mechanical characterization of epoxy composites modified with reactive polyol diluent and randomly-oriented amino-functionalized MWCNTs. *Polymer Testing* **31**, 1083–1093 (2012).
29. L.-C. Tang, Y.-J. Wan, D. Yan, Y.-B. Pei, L. Zhao, Y.-B. Li, L.-B. Wu, J.-X. Jiang, G.-Q. Lai, The effect of graphene dispersion on the mechanical properties of graphene/epoxy composites. *Carbon* **60**, 16–27 (2013).
30. T. Ramanathan, A. A. Abdala, S. Stankovich, D. A. Dikin, M. Herrera-Alonso, R. D. Piner, D. H. Adamson, H. C. Schniepp, X. Chen, R. S. Ruoff, S. T. Nguyen, I. A. Aksay, R. K. Prud'Homme, L. C. Brinson, Functionalized graphene sheets for polymer nanocomposites. *Nat. Nanotech.* **3**, 327–331 (2008).
31. J. R. Potts, D. R. Dreyer, C. W. Bielawski, R. S. Ruoff, Graphene-based polymer nanocomposites. *Polymer* **52**, 5–25 (2011).
32. S.-Y. Fu, X.-Q. Feng, B. Lauke, Y.-W. Mai, Effects of particle size, particle/matrix interface adhesion and particle loading on mechanical properties of particulate–polymer composites. *Compos. Part B Eng.* **39**, 933–961 (2008).
33. R. O. Ritchie, The conflicts between strength and toughness. *Nat. Mater.* **10**, 817–822 (2011).
34. T. D. Ngo, A. Kashani, G. Imbalzano, K. T. Q. Nguyen, D. Hui, Additive manufacturing (3D printing): A review of materials, methods, applications and challenges. *Compos. Part B Eng.* **143**, 172–196 (2018).
35. A. Maguire, N. Pottackal, M. A. S. R. Saadi, M. M. Rahman, P. M. Ajayan, Additive manufacturing of polymer-based structures by extrusion technologies. *Oxford Open Mater. Sci.* **1**, itaa004 (2020).
36. J. A. Lewis, Direct ink writing of 3D functional materials. *Adv. Funct. Mater.* **16**, 2193–2204 (2006).
37. M. A. S. R. Saadi, A. Maguire, N. Pottackal, M. S. H. Thakur, M. M. Ikram, A. J. Hart, P. M. Ajayan, M. M. Rahman, Direct ink writing: A 3D printing technology for diverse materials. *Adv. Mater.* **34**, 2108855 (2022).

38. N. S. Hmeidat, J. W. Kemp, B. G. Compton, High-strength epoxy nanocomposites for 3D printing. *Compos. Sci. Technol.* **160**, 9–20 (2018).
39. Y. Liu, J. Lu, Y. Cui, Improved thermal conductivity of epoxy resin by graphene–Nickel three-dimensional filler. *Carbon Res. Conversion* **3**, 29–35 (2020).
40. C. Huang, X. Qian, R. Yang, Thermal conductivity of polymers and polymer nanocomposites. *Mater. Sci. Eng. R Rep.* **132**, 1–22 (2018).
41. W. Guo, G. Chen, Fabrication of graphene/epoxy resin composites with much enhanced thermal conductivity via ball milling technique. *J. Appl. Polym. Sci.* **131**, 40565 (2014).
42. S. M. Sajadi, S. Enayat, L. Vásárhelyi, A. Alabastri, M. Lou, L. M. Sassi, A. Kutana, S. Bhowmick, C. Durante, Á. Kukovecz, A. B. Puthirath, Z. Kónya, R. Vajtai, P. Boul, C. S. Tiwary, M. M. Rahman, P. M. Ajayan, Three-dimensional printing of complex graphite structures. *Carbon* **181**, 260–269 (2021).
43. S.-L. Chung, J.-S. Lin, Thermal conductivity of epoxy resin composites filled with combustion synthesized h-BN particles. *Molecules* **21**, 670 (2016).
44. A. Yu, M. E. Itkis, E. Bekyarova, R. C. Haddon, Effect of single-walled carbon nanotube purity on the thermal conductivity of carbon nanotube-based composites. *Appl. Phys. Lett.* **89**, 133102 (2006).
45. F. Wang, L. T. Drzal, Y. Qin, Z. Huang, Mechanical properties and thermal conductivity of graphene nanoplatelet/epoxy composites. *J. Mater. Sci.* **50**, 1082–1093 (2015).
46. G. V. Kaliyannan, M. K. K. Velusamy, S. K. Palaniappan, M. K. Anandraj, R. Rathanasamy, Polymer coatings for corrosive protection, in *Polymer Coatings*, Inamuddin, R. Boddula, M. I. Ahamed, A. M. Asiri, Eds. (Wiley, ed. 1, 2020; https://onlinelibrary.wiley.com/doi/10.1002/9781119655145.ch17), pp. 371–395.
47. G. Chilkoor, R. Sarder, J. Islam, K. E. ArunKumar, I. Ratnayake, S. Star, B. K. Jasthi, G. Sereda, N. Koratkar, M. Meyyappan, V. Gadhamshetty, Maleic anhydride-functionalized graphene nanofillers render epoxy coatings highly resistant to corrosion and microbial attack. *Carbon* **159**, 586–597 (2020).
48. G. Marlair, C. Cwiklinski, A. Tewarson, "An analysis of some practical methods for estimating heats of combustion in fire safety studies," paper presented at the 8th, INTERFLAM '99: Fire science and engineering conference, Edinburgh, UK, 01 January 1999.
49. T. Gibon, Á. H. Menacho, M. Guiton, *Life Cycle Assessment of Electricity Generation Options* (United Nations Economic Commission for Europe, 2021).
50. W. A. Algozeeb, P. E. Savas, D. X. Luong, W. Chen, C. Kittrell, M. Bhat, R. Shahsavari, J. M. Tour, Flash graphene from plastic waste. *ACS Nano* **14**, 15595–15604 (2020).
51. X. Wang, H. You, F. Liu, M. Li, L. Wan, S. Li, Q. Li, Y. Xu, R. Tian, Z. Yu, D. Xiang, J. Cheng, Large-scale synthesis of few-layered graphene using CVD. *Chem. Vap. Deposition* **15**, 53–56 (2009).
52. S. Dayou, B. Vigolo, A. Desforges, J. Ghanbaja, A. R. Mohamed, High-rate synthesis of graphene by a lower cost chemical vapor deposition route. *J. Nanopart. Res.* **19**, 336 (2017).
53. C. Shan, H. Tang, T. Wong, L. He, S.-T. Lee, Facile synthesis of a large quantity of graphene by chemical vapor deposition: An advanced catalyst carrier. *Adv. Mater.* **24**, 2491–2495 (2012).
54. Y. Shen, A. C. Lua, A facile method for the large-scale continuous synthesis of graphene sheets using a novel catalyst. *Sci. Rep.* **3**, 3037 (2013).
55. M. Kowalik, C. Ashraf, B. Damirchi, D. Akbarian, S. Rajabpour, A. C. T. van Duin, Atomistic scale analysis of the carbonization process for C/H/O/N-based polymers with the ReaxFF reactive force field. *J. Phys. Chem. B* **123**, 5357–5367 (2019).
56. Y. L. F. Musico, C. M. Santos, M. L. P. Dalida, D. F. Rodrigues, Surface modification of membrane filters using graphene and graphene oxide-based nanomaterials for bacterial inactivation and removal. *ACS Sustain. Chem. Eng.* **2**, 1559–1565 (2014).
57. G. Wernet, C. Bauer, B. Steubing, J. Reinhard, E. Moreno-Ruiz, B. Weidema, The ecoinvent database version 3 (part I): Overview and methodology. *Int. J. Life Cycle Assess.* **21**, 1218–1230 (2016).
58. K. Qian, K. E. Edwards, M. Siskin, W. N. Olmstead, A. S. Mennito, G. J. Dechert, N. E. Hoosain, Desorption and ionization of heavy petroleum molecules and measurement of molecular weight distributions. *Energy Fuels* **21**, 1042–1047 (2007).
59. M. Siskin, S. R. Kelemen, M. L. Gorbaty, M. Afeworki, L. D. Brown, D. T. Ferrughelli, R. J. Kennedy, Asphaltene molecular structure and chemical influences on the morphology of coke produced in delayed coking. *Energy Fuels* **20**, 1227–1234 (2006).
60. J. M. Sheremata, M. R. Gray, H. D. Dettman, W. C. McCaffrey, Quantitative molecular representation and sequential optimization of Athabasca asphaltenes. *Energy Fuels* **18**, 1377–1384 (2004).
61. S. Hosokai, K. Matsuoka, K. Kuramoto, Y. Suzuki, Modification of Dulong's formula to estimate heating value of gas, liquid and solid fuels. *Fuel Process. Technol.* **152**, 399–405 (2016).
62. L. S. Lin, W. Bin-Tay, Z. Aslam, A. V. K. Westwood, R. Brydson, Determination of the lateral size and thickness of solution-processed graphene flakes. *J. Phys.: Conf. Ser.* **902**, 012026 (2017).
63. A. Shimamura, Y. Hotta, H. Hyuga, M. Hotta, K. Hirao, Improving the thermal conductivity of epoxy composites using a combustion-synthesized aggregated β-Si3N4 filler with randomly oriented grains. *Sci. Rep.* **10**, 14926 (2020).
64. R. K. Pachauri, L. A. Meyer, Climate Change 2014: Synthesis Report. Contribution of Working Groups I, II and III to the Fifth Assessment Report of the Intergovernmental Panel on Climate Change (IPCC, Geneva, Switzerland, 2014).
65. S. Payen, Eutrophication Potential Indicators in LCA (2016).
66. L. van Oers, J. Guinée, The abiotic depletion potential: Background, updates, and future. *Resources* **5**, 16 (2016).
67. J. B. Guinée, R. Heijungs, H. A. Udo de Haes, G. Huppes, Quantitative life cycle assessment of products. 2. Classification, valuation and improvement analysis. *J. Clean. Prod.* **1**, 81–91 (1993).
68. R. K. Rosenbaum, T. M. Bachmann, L. S. Gold, M. A. J. Huijbregts, O. Jolliet, R. Juraske, A. Koehler, H. F. Larsen, M. MacLeod, M. Margni, T. E. McKone, J. Payet, M. Schuhmacher, D. Van De Meent, M. Z. Hauschild, USEtox—The UNEP-SETAC toxicity model: Recommended characterisation factors for human toxicity and freshwater ecotoxicity in life cycle impact assessment. *Int. J. Life Cycle Assess.* **13**, 532–546 (2008).
69. M. J. Goedkoop, "The Eco-indicator 99—A damage-oriented method for life cycle impact assessment methodology report" (Pre Consultants, 1999).
70. D. Peterson, J. Vickers, D. DeSantis, "Hydrogen production cost from PEM electrolysis – 2019" (Tech. Rep. Record-19009, US Department of Energy, 2020).

Acknowledgments: We are grateful to Alessandro Alabastri for helpful discussion on finite element modeling of laser heating. The characterization equipment used in this project is from the Shared Equipment Authority (SEA) at Rice University. **Funding:** The authors gratefully acknowledge financial support from Alberta Innovates for Carbon Fiber Grand Challenge Phase I and Phase II programs. The work at Rice University was funded by Air Force Office of Scientific Research (FA9550-19-1-0296, J.M.T.) and the U.S. Army Corps of Engineers, ERDC (W912HZ-21-2-0050, J.M.T.). V.G. acknowledges the funding support from the NSF RII FEC awards (#1849206 and #1920954). **Author contributions:** M.A.S.R.S. and M.M.R. conceived and coordinated the research. M.A.S.R.S. conducted TGA, XPS, and XRD experiments of asphaltene and AFG; fabricated the composites; conducted mechanical testing and SEM imaging of fracture surface; and analyzed the thermal data. P.A.A. performed the FJH experiments and TEM characterizations. M.S.H.T. analyzed the mechanical testing data, performed the rheology experiments, and conducted the FEM simulations. A.K. 3D-printed the nanocomposite samples. S.S. and A.S.Z. analyzed the XPS data. S.K.N. conducted the LCA study. A.Z. assisted in the processing of asphaltene and composite fabrication. S.R. assisted in XPS experiment. M.L. performed the laser heating experiments. S.N.B. and V.G. conducted the corrosion tests and analysis. M.A.A.B. did the TEA analysis. Y.Z. and A.V. performed the MD simulations. J.L.B. did the Raman experiments and analysis. All authors analyzed and discussed the results. M.A.S.R.S. and M.S.H.T. wrote the manuscript. M.G.K., J.M.T., P.M.A., and M.M.R. supervised the project, reviewed and edited the manuscript, and were responsible for funding acquisition. **Competing interests:** Rice University owns intellectual property on the FJH process for the conversion of carbon sources, including asphaltenes into graphene. That intellectual property has been licensed to Universal Matter Inc. and Universal Matter Ltd. J.M.T. owns stock in these companies, but he is not an officer, employee, or director therein. All conflicts of interest are managed through regular disclosure to the Rice University Office of Sponsored Programs and Research Compliance. The authors declare that they have no other competing interests. **Data and materials availability:** All data needed to evaluate the conclusions in the paper are present in the paper and/or the Supplementary Materials.

Submitted 7 June 2022
Accepted 30 September 2022
Published 18 November 2022
10.1126/sciadv.add3555